

# 000 001 002 003 004 005 006 007 008 009 010 011 012 013 014 015 016 017 018 019 020 021 022 023 024 025 026 027 028 029 030 031 032 033 034 035 036 037 038 039 040 041 042 043 044 045 046 047 048 049 050 051 052 053 IMPLICIT 4D GAUSSIAN SPLATTING FOR FAST MOTION WITH LARGE INTER-FRAME DISPLACEMENTS

Anonymous authors

Paper under double-blind review

## ABSTRACT

Recent 4D Gaussian Splatting (4DGS) methods often fail under fast motion with large inter-frame displacements, where Gaussian attributes are poorly learned during training, and fast-moving objects are often lost from the reconstruction. In this work, we introduce Spatiotemporal Position Implicit Network for 4DGS, coined SPIN-4DGS, which learns Gaussian attributes from explicitly collected spatiotemporal positions rather than modeling temporal displacements, thereby enabling more faithful splatting under fast motions with large inter-frame displacements. To avoid the heavy memory overhead of explicitly optimizing attributes across all spatiotemporal positions, we instead predict them with a lightweight feed-forward network trained under a rasterization-based reconstruction loss. Consequently, SPIN-4DGS learns shared representations across Gaussians, effectively capturing spatiotemporal consistency and enabling stable high-quality Gaussian splatting even under challenging motions. Across extensive experiments, SPIN-4DGS consistently achieves higher fidelity under large displacements, with clear improvements in PSNR and SSIM on challenging sports scenes from the CMU Panoptic dataset. For example, SPIN-4DGS notably outperforms the strongest baseline, D3DGS, by achieving +1.83 higher PSNR on the Basketball scene.

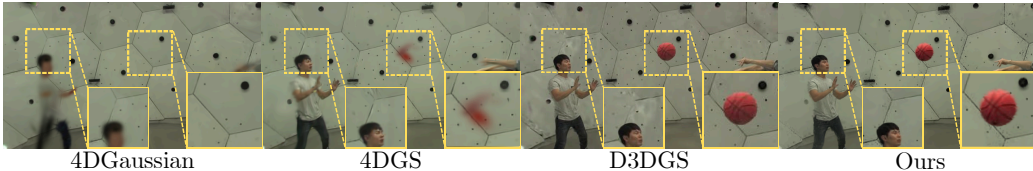


Figure 1: **Faithful reconstruction of fast motion with large inter-frame displacements.** Existing 4DGS approaches often produce blurred or incomplete reconstructions of fast-moving objects. In contrast, ours successfully reconstructs clear and accurate details, such as the basketball in the scene.

## 1 INTRODUCTION

Rendering fast motions with large inter-frame displacements remains challenging for dynamic scene reconstruction, despite its importance for a wide range of real-world applications. Recent advances in 4D Gaussian Splatting (4DGS) have shown remarkable efficiency and visual quality, making it a promising framework for dynamic scene reconstruction. In particular, existing 4DGS methods (Yang et al., 2024a; Duan et al., 2024; Wu et al., 2024; Xu et al., 2024) achieves strong results on dynamic scenes with small displacements (*e.g.*, Neu3D (Li et al., 2022b)) across video frames.

However, as motions become faster and inter-frame shifts grow larger (*e.g.*, Panoptic Sports (Joo et al., 2015)), existing 4DGS methods, including explicit 4D parametrization (Yang et al., 2024a; Duan et al., 2024) and deformable approaches (Wu et al., 2024; Xu et al., 2024; Kwak et al., 2025), often fail to capture the rapid dynamics, producing blurred or even vanished objects. To be specific, in deformable approaches, Gaussians are defined in a static canonical space and transformed over time through learned deformations. However, they often fail to assign initial Gaussians for fast-moving objects in the canonical space, causing those objects to remain unseen during deformation training. On the other hand, although explicit parameterization roughly tracks Gaussian positions that correspond to fast motions at the early stage of training, their attributes, including color, opacity,

054  
055  
056  
057  
058  
059(a) **Left:** 15K training iteration, **Right:** 30K training iteration.

(b) Canonical space

Figure 2: **Failure modes on fast motions with large inter-frame displacements.** We visualize failure modes of existing frameworks; (2a) explicit parameterization and (2b) deformable methods. Figure (2a) shows drastic degradation on training iterations (*i.e.*, 15K  $\rightarrow$  30K), and (2b) shows the canonical space of deformable initialization fails to assign Gaussians for fast motions.

scale, and rotation, rapidly collapse in later training, leading to drastic degradation. As a result, both approaches show failure modes with blurred or even vanished motions, as shown in Figure 2.

To this end, we focus on addressing the failure in learning Gaussian attributes for fast-moving objects with large displacements. Although positions remain sufficiently accurate to capture motion, other attributes collapse more easily. This degradation arises because reconstruction loss is dominated by background Gaussians; fast-moving Gaussians at new positions incur higher reconstruction errors, while static backgrounds are easier to fit. As a result, both deformable and explicit 4DGS approaches tend to bias learning toward background fitting, eventually leading dynamic objects to disappear. In addition, such large displacements can cause cross-frame interference during frame-by-frame rasterization. Although a 4DGS (Yang et al., 2024a) can be sliced differently at each time, its parameters are shared, so optimizing for one frame makes other slices suboptimal unless we separate Gaussians by explicit spatiotemporal positions  $(x, y, z, t)$ . This observation motivates us to leverage the explicit spatiotemporal positions of fast-moving Gaussians as inputs for generating their attributes, thereby achieving more faithful splatting under large displacements.

In this paper, we introduce SPIN-4DGS (Spatiotemporal Position Implicit Network for 4DGS), a lightweight yet effective framework designed to handle fast motions with large inter-frame displacements. To be specific, we first estimate high-quality spatiotemporal positions  $(x, y, z, t)$  of Gaussians that can serve as the inputs for later attribute prediction, initially gathering them across the entire scene before refining them in a frame-wise manner. Then, we leverage these positions to predict Gaussian attributes through a lightweight feed-forward network, avoiding the heavy memory overhead of explicitly optimizing attributes over all spatiotemporal positions. This design learns a shared implicit representation across all Gaussians and decodes attributes directly from positions under rasterization loss. As a result, learned attributes remain consistent across positions, and dynamic objects can stay stable even under large displacements. Meanwhile, attributes are stored implicitly in network parameters, rather than explicitly for each Gaussian, which significantly improves memory efficiency on a large number of spatiotemporal positions.

To validate the effectiveness of the proposed SPIN-4DGS, we perform experiments on various sports scenes from the CMU Panoptic Sports dataset, where human motions are rapid and small objects move across large inter-frame displacements. Across six sports scenes, SPIN-4DGS achieves the best performances, significantly outperforming all baselines. For example, SPIN-4DGS achieves a +1.83 PSNR dB improvement compared to the strongest baseline, D3DGS (Luiten et al., 2024), with a higher SSIM of 0.92 on the Basketball scene. Specifically, qualitative results in Figure 4 and Table 1 demonstrate that prior methods often blur Gaussians or fail to capture fast-moving objects (*e.g.*, Basketball), whereas SPIN-4DGS preserves them with sharp and stable reconstructions. Interestingly, we further observe that SPIN-4DGS significantly improves performance when reusing pre-trained Gaussian positions from strong baselines, such as D3DGS (Luiten et al., 2024) and 4DGS (Yang et al., 2024a).

Overall, our work introduces SPIN-4DGS, the first framework that learns Gaussian attributes directly from **jointly optimized frame-wise positions**, enabling stable and high-quality 4DGS under large inter-frame displacements. **This 4D reparameterization allows ours to mitigate temporal failure modes under such fast motion while still capturing rich temporal appearance dynamics.** We believe SPIN-4DGS addresses a fundamental challenge of 4DGS by enabling stable learning in various real-world scenarios, thereby opening a new direction for advancing dynamic scene representation.

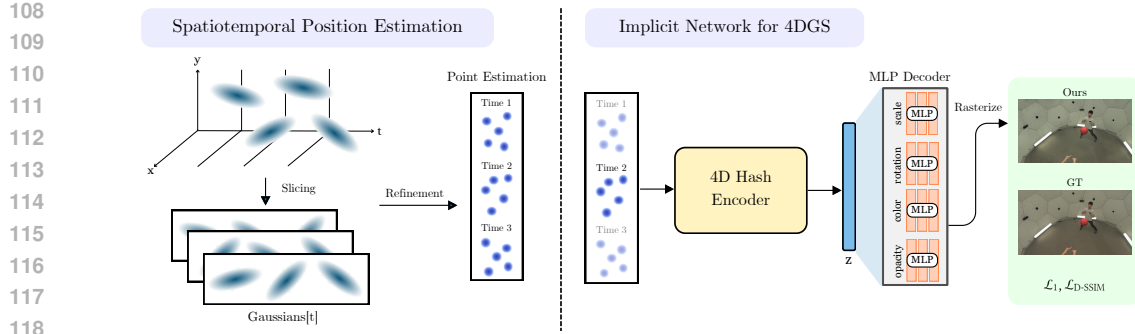


Figure 3: **Illustration of the overall framework.** SPIN-4DGS consists of two stages of (a) Spatiotemporal Position Estimation and (b) Implicit Network for 4DGS. Specifically, (a) we slice Gaussians along the temporal axis to obtain spatiotemporal position sets and refine them with rasterization loss. Then, (b) the refined positions are normalized and passed through a 4D hash encoder and multi-branch decoders to predict Gaussian attributes (scale, rotation, color, and opacity).

## 2 RELATED WORK

**Learning temporal dynamics for 3D Gaussian.** Recent advances have shown significant progress in extending 3D Gaussian representations into the 4D domain by learning temporal dynamics. Early attempts (Luiten et al., 2024; Javed et al., 2024) incrementally propagated 3D Gaussians from the first frame, demonstrating the potential of 4D Gaussian splatting, but suffering from sequential inefficiency and overfitting due to numerous per-frame iterations. However, their reliance on external supervision, such as segmentation masks, substantially increases training costs and computational overhead. Meanwhile, inspired by NeRF approaches (Cao & Johnson, 2023; Fridovich-Keil et al., 2023; Park et al., 2021), deformable frameworks (Wu et al., 2024; Yang et al., 2024b; Lu et al., 2024; Zhu et al., 2024; Lin et al., 2024; Xu et al., 2024) instead construct a canonical space to initialize Gaussians and then learn temporal displacements in rotation, scale, and position. Despite their robustness on motions with small inter-frame displacements, these methods still underperform on rapid motions with large displacements, as Gaussians that represent fast motion are often omitted during canonicalization and thus remain unseen in the subsequent deformation process. In contrast, we address these challenges without external supervision, showing that high-fidelity capture of fast motion can be achieved solely from raw video inputs.

**Explicit 4D Gaussian Parameterizations.** Another promising direction is to focus on directly parameterizing Gaussians in 4D from scratch (Yang et al., 2024a; Lee et al., 2024; Duan et al., 2024), rather than optimizing each frame separately in the 3D domain. Such explicit 4D modeling unifies space and time into a continuous field and encodes dynamics as 4D Gaussian splats, which can be temporally sliced for rendering, in contrast to deformable-based approaches. For instance, 4D-Rotor-Gaussians (Duan et al., 2024) performs temporal slicing of 4D Gaussians at each timestamp to obtain dynamic 3D Gaussians, which are then projected to the image plane. While explicit 4D parameterizations achieve higher frame rates (FPS) and improved rendering quality, they require longer training times and larger storage requirements. Moreover, under fast motion with large displacements, we observed that corresponding Gaussian attributes gradually blur due to cross-frame interference. A single 4D Gaussian must simultaneously explain all timestamps; however, rasterization is performed frame by frame, so optimization for one frame inevitably affects the others. This inherent conflict in the rasterization process makes it challenging to maintain temporal consistency in dynamic regions. In contrast, our method avoids such cross-frame degradation by directly decoding Gaussians at explicit spatiotemporal positions in a feed-forward manner. This design explicitly separates large-displacement Gaussians at each timestamp, which prevents cross-frame degradation and leads to both stable training and consistent rendering quality.

## 3 METHOD

In this section, we present the Spatiotemporal Position Implicit Network for 4DGS (SPIN-4DGS), a framework for reconstructing dynamic scenes under motions with large inter-frame displacements.

We first review 3D Gaussian Splatting as preliminaries in section 3.1. Then, section 3.2 describes how we obtain explicit spatiotemporal Gaussian positions, and section 3.3 details how their attributes are predicted via a feed-forward implicit network. The overall framework is illustrated in Figure 3.

### 3.1 PRELIMINARY: 3D GAUSSIAN SPLATTING

3D Gaussian Splatting (3DGS; Kerbl et al. (2023)) provides a differentiable volume rendering representation. It introduces anisotropic Gaussians where the parameters (*i.e.*, position, scale, rotation, color, and opacity) of each Gaussian are defined and optimized for tile-based rendering. Structure-from-Motion (SfM; Schonberger & Frahm (2016)) techniques estimate the initial positions and colors of Gaussians from input images. For a given arbitrary point  $\mathbf{x} \in \mathbb{R}^3$  in the 3D scene, Gaussian is defined as follows:

$$G^{3D}(\mathbf{x}) = \exp\left(-\frac{1}{2}(\mathbf{x} - \boldsymbol{\mu})^\top \boldsymbol{\Sigma}_{3D}^{-1}(\mathbf{x} - \boldsymbol{\mu})\right), \quad (1)$$

where  $G^{3D}(\mathbf{x})$  denotes the value of the Gaussian at arbitrary point  $\mathbf{x}$ . The parameters of each Gaussian include the position  $\boldsymbol{\mu} \in \mathbb{R}^3$ , opacity  $o \in \mathbb{R}$ , color  $\mathbf{c} \in \mathbb{R}^3$  represented using spherical harmonics coefficients, and the covariance matrix  $\boldsymbol{\Sigma} \in \mathbb{R}^{3 \times 3}$ , which is defined in terms of a diagonal scale matrix  $\mathbf{S} = \text{diag}(s_1, s_2, s_3)$  and a rotation matrix  $\mathbf{R} \in \text{SO}(3)$ , obtained from quaternions. To ensure that the covariance matrix remains  $\boldsymbol{\Sigma}$  positive semi-definite, it is computed as follows:

$$\boldsymbol{\Sigma}_{3D} = \mathbf{R} \mathbf{S} \mathbf{S}^\top \mathbf{R}^\top. \quad (2)$$

To render via rasterization, the 3D Gaussians are first projected onto the 2D image plane. This is done by applying the viewing transformation  $\mathbf{W}$  and the Jacobian matrix (Zwicker et al., 2001)  $\mathbf{J}$  to compute the 2D covariance matrix  $\boldsymbol{\Sigma}_{2D}$  as follows:

$$\boldsymbol{\Sigma}_{2D} = \mathbf{J} \mathbf{W} \boldsymbol{\Sigma}_{3D} \mathbf{W}^\top \mathbf{J}^\top \quad (3)$$

During the rendering process, pixel values are computed via alpha blending. The alpha value (*i.e.*, opacity) of each Gaussian is obtained by projecting the 3D Gaussian  $G_i$  into 2D as  $G_i^{2D}$ . Specifically, for each pixel, the alpha value  $\alpha'_i$  and the resulting color  $\mathbf{C}$  are computed as

$$\alpha'_i = o_i G_i^{2D}(\mathbf{x}), \quad \mathbf{C}(\mathbf{x}) = \sum_{i=1}^N c_i \alpha'_i \prod_{j=1}^{i-1} (1 - \alpha'_j), \quad (4)$$

where  $o_i$  is the intrinsic opacity of the  $i$ -th Gaussian,  $c_i$  its color, and  $N$  the total number of Gaussians contributing to the pixel.

### 3.2 SPATIOTEMPORAL GAUSSIAN POSITIONS

In this section, our goal is to construct a Gaussian point set that fully spans the trajectory of dynamic objects, ensuring sufficient coverage for faithful reconstruction. Prior methods perform reasonably well in regions where Gaussians are densely clustered, but under large inter-frame displacements, they often fail to maintain enough points around fast-moving objects. Even when positions are sufficiently available, attributes remain challenging. To be specific, when Gaussians spanning the entire trajectory are optimized jointly, frame-specific supervision signals interfere with one another. Because rasterization is performed frame by frame, updates that make a Gaussian optimal for one timestamp can render it suboptimal for others. This cross-frame interference can potentially weaken the learning signal and degrade the quality of the reconstruction.

To overcome these issues, we construct Gaussian sets independently at each time step, explicitly separating them by spatiotemporal positions. This formulation avoids interference across frames and enables more reliable attribute learning for fast-moving objects under large displacements.

$$u_t = f_\theta(\mathbf{x}, \mathbf{y}, \mathbf{z}, \mathbf{t}), \quad \mathbf{c}_t = g_\phi(\mathbf{x}, \mathbf{y}, \mathbf{z}, \mathbf{t}) \in \{0, \dots, 255\}^3, \quad t \in \{1, \dots, T\}. \quad (5)$$

Here,  $f_\theta$  and  $g_\phi$  are explicit functions of the temporal axis predicting the position and color corresponding to each frame  $t$ . For example, the explicit approaches (Duan et al., 2024; Yang et al., 2024a) construct points by performing time slicing along the temporal axis, whereas a deformable approach (Wu et al., 2024; Xu et al., 2024; Bae et al., 2024) network can learn to construct them

as time-varying structures. For SPIN-4DGS, we estimate spatiotemporal positions by an explicit method (Yang et al., 2024a) as a default. Lastly, we further refine the estimated position by utilizing rasterization loss with corresponding colors at every frame to densify salient points and prune unnecessary ones.

$$u_t \leftarrow \text{Refine}(u_t, \mathbf{c}_t; t), \quad t = 0, \dots, T. \quad (6)$$

After refinement, the Gaussian points at each timestamp  $t$  are fixed as explicit spatiotemporal positions and directly fed into our implicit network to learn the corresponding attributes.

### 3.3 IMPLICIT NETWORK FOR 4D GAUSSIAN SPLATTING

In this section, we describe an implicit network that is trained in an end-to-end manner to directly predict 4D Gaussian parameters from learnable spatiotemporal Gaussian positions initialized from the collected ones. In contrast to prior approaches require pre-defined or pre-optimized Gaussian attributes (e.g., scale, rotation, opacity, color) to model temporal dynamics, our network is trained from scratch using only the collected spatiotemporal positions  $(\mu, t) \in \mathbb{R}^4$  as input. Given  $(\mu, t)$ , the network predicts all 4D Gaussian parameters, including opacity  $o \in \mathbb{R}^1$ , spherical harmonics coefficients  $sh \in \mathbb{R}^{48}$ , scale  $s \in \mathbb{R}^3$ , and rotation represented as a unit quaternion  $\mathbf{r} \in \mathbb{R}^4$ .

**Input position normalization.** At each frame  $t$ , the spatiotemporal Gaussian positions serve as inputs to a feed-forward network for learning implicit representations of other Gaussian parameters. Since the raw 3D Gaussian positions  $\mathbf{u} \in \mathbb{R}^3$  on the scene are unbounded, we apply a normalization step to stabilize learning and preserve representational capacity. Specifically, following the scene contraction strategy of Mip-NeRF (Barron et al., 2021), we first compress the coordinates into a finite ball and then map them to the normalized range  $[0, 1]^3$ , as defined in equation 7.

$$\text{contract}(\mu) = \begin{cases} \mu, & \|\mu\| \leq 1, \\ \left(2 - \frac{1}{\|\mu\|}\right) \frac{\mu}{\|\mu\|}, & \|\mu\| > 1, \end{cases} \quad \bar{\mu} = \frac{1}{4} \text{contract}(\mu) + \frac{1}{2} \in [0, 1]^3. \quad (7)$$

To keep spatial and temporal scales comparable, we normalize time to  $[0, 1]$  to match the scale of the spatial embedding. Concretely, we use the current timestamp divided by the total duration:

$$t_{\text{norm}} = \frac{t - t_{\min}}{t_{\max} - t_{\min}} \in [0, 1] \quad \text{and} \quad \tilde{\mathbf{x}} = [\bar{\mu}^\top, t_{\text{norm}}]^\top \in [0, 1]^4. \quad (8)$$

Our network adopts an encoder-decoder architecture, where the encoder  $f_{\text{enc}}$  maps the normalized input  $\tilde{\mathbf{x}}$  to a latent embedding  $f_{\text{enc}}(\tilde{\mathbf{x}})$  which the decoder takes as input. We note that the position  $\mathbf{u}$  is also parameterized and jointly optimized with the network, similar to existing frameworks (Wu et al., 2024; Xu et al., 2024).

**Encoder architecture for shared latent representation.** We directly extend the widely used 3D Instant-NGP (Müller et al., 2022) multi-hash grid to 4D by appending the temporal axis, producing a compact latent vector for each input. Given the normalized input  $\tilde{\mathbf{x}} = [\bar{\mu}^\top, t_{\text{norm}}]^\top$ , we map it into a unified 4D embedding via a single spatio-temporal encoder. In contrast to low-rank decompositions (e.g., planar), which may reduce computation but degrade expressiveness as the number of Gaussians grows and incur extra cost from per-level hash management, we avoid such factorizations and employ the 4D hash encoder (Chen et al., 2025) directly as follows:

$$z = f_{\text{enc}}(\tilde{\mathbf{x}}) \in \mathbb{R}^{LF} \quad (9)$$

where  $L$  denotes the number of hash levels and  $F$  the number of channels per level. We concatenate features across all levels to form  $z \in \mathbb{R}^{LF}$ , which we use as the latent representation.

**Attribute-aware decoder for Gaussian attribute prediction.** Given a latent vector  $\mathbf{z}$ , we use a multi-branch decoder to produce Gaussian parameters, scale, rotation, spherical harmonics coefficients, and opacity. Each attribute is predicted by a separate head (three-layer MLP) taking the shared encoder output  $\mathbf{z} \in \mathbb{R}^{LF}$  as input. All decoder heads use GELU (Hendrycks & Gimpel, 2016) activations instead of ReLU (Agarap, 2018).

$$(\hat{\mathbf{s}}, \hat{\mathbf{r}}, \hat{\mathbf{sh}}, \hat{\mathbf{o}}) = (f_{\text{scale}}(\mathbf{z}), f_{\text{rot}}(\mathbf{z}), f_{\text{sh}}(\mathbf{z}), f_{\text{opacity}}(\mathbf{z})). \quad (10)$$

270 We convert the raw outputs into valid parameter ranges using attribute-specific activations and post-  
 271 processing:  
 272

$$273 \quad (\mathbf{s}, \mathbf{r}, \mathbf{sh}, \mathbf{o}) = \left( \exp(\hat{\mathbf{s}}), \frac{\hat{\mathbf{r}}}{\|\hat{\mathbf{r}}\|_2}, \hat{\mathbf{sh}}, \sigma(\hat{\mathbf{o}}) \right). \quad (11)$$

274 We also follow the Gaussian post-processing (Kerbl et al., 2023) pipeline, with a few additional  
 275 steps for stable training.  
 276

277 **Scale decoder.** To prevent gradient explosion from exponential growth, we clip the pre-scale in the  
 278 backward pass:  $\hat{s} \leftarrow \text{clip}(\hat{s}, \text{max} = 20)$ . We also initialize the final-layer bias to  $-5$  to start from a  
 279 small scale, *i.e.*,  $\exp(-5) \approx 0.0067$ , and keep it trainable.

280 **Rotation decoder.** To bias the predicted quaternion toward the identity at the start of training, we  
 281 set the final-layer bias to  $(1, 0, 0, 0)$ , *i.e.*, the first element to 1.0 and the remaining elements to 0,  
 282 so that the initial output satisfies  $\hat{\mathbf{r}} \approx (1, 0, 0, 0)$ . This initialization lets the network learn rotations  
 283 progressively while preserving a stable initial structure.

284 **Opacity decoder.** To stabilize early training and encourage a near-transparent start, we set the  
 285 final-layer bias to  $\text{logit}(0.1) \approx -2.197$  (trainable), initializing  $\hat{o}$  at  $\approx 0.1$ . The network then learns  
 286 to increase opacity only where needed, focusing on informative points.  
 287

288 **Color decoder.** The decoder directly regresses color coefficients from encoder embeddings, with  
 289 no special initialization, to capture the high-dimensional color required for SH-based rendering.  
 290

291 **Loss objectives.** Finally, frame images are rendered via rasterization, and we optimize the model  
 292 using the standard 3DGS reconstruction loss as follows:  
 293

$$294 \quad \mathcal{L} = (1 - \lambda) \mathcal{L}_1 + \lambda \mathcal{L}_{\text{D-SSIM}}. \quad (12)$$

295 where  $\lambda$  is a hyperparameter; we set  $\lambda = 0.2$ , as following prior works (Kerbl et al., 2023).  
 296

## 297 4 EXPERIMENTS

298 In this section, we demonstrate the effectiveness of the proposed method, SPIN-4DGS. Specifically,  
 299 we choose to employ the recent explicit parameterization method for 4DGS (Yang et al., 2024a),  
 300 which is publicly available, only in the early training stage to estimate spatiotemporal Gaussian  
 301 positions. These positions are then used in our framework to learn new Gaussian attributes. We  
 302 then evaluate its ability to capture fast motion on various sports scene benchmarks from the CMU  
 303 Panoptic Sports dataset (Joo et al., 2015), comparing it with existing 4DGS baselines.  
 304

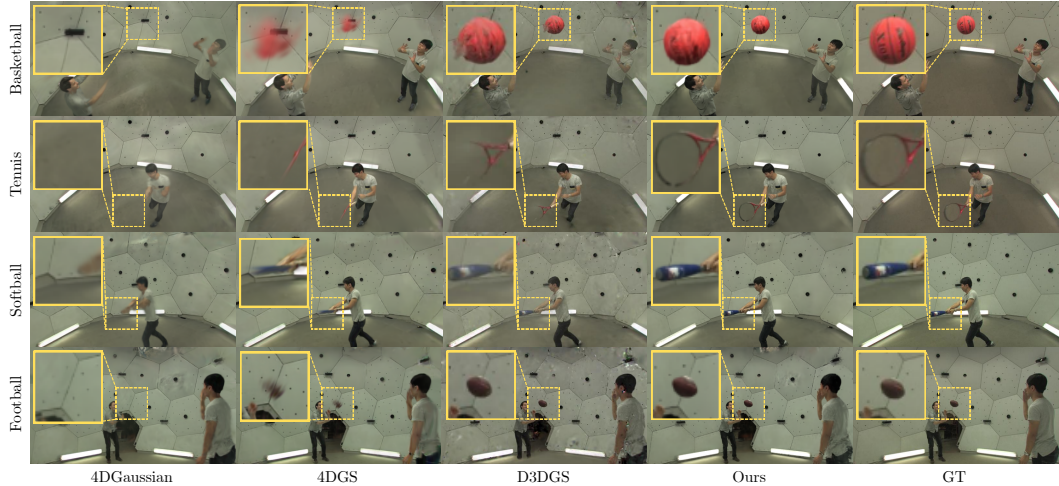
305 **Implementation details.** The network uses a hidden dimension of 64, and the encoder is configured  
 306 with  $L = 16$  levels and  $F = 4$  features per level; the hash map size 21. Parameter groups in  
 307 both the encoder and the decoder utilize separate learning rates, as Gaussian attributes (*e.g.*, scale  
 308 and rotation) are sensitive, and a uniform learning rate often leads to unstable optimization. The  
 309 encoder learning rate is initialized to  $8 \times 10^{-3}$ ; decoder learning rates are  $1 \times 10^{-3}$  for color,  
 310  $3 \times 10^{-4}$  for scale,  $3 \times 10^{-5}$  for rotation, and  $8 \times 10^{-4}$  for opacity. position parameters use the  
 311 same learning rate as 3DGS. We use Adam (Kinga et al., 2015) with a linear warm-up and cosine  
 312 decay schedule, under which every parameter’s learning rate decays to  $1 \times 10^{-7}$ . Experiments  
 313 were conducted on an RTX 4090 GPU (24 GB), and the implementation utilized PyTorch (Paszke  
 314 et al., 2019) 2.1 with CUDA 11.8. By default, we train for 40K iterations with a batch size of 3.  
 315 We perform quantitative evaluations using PSNR (Peak Signal-to-Noise Ratio), SSIM (Wang et al.  
 316 (2004); Structural Similarity Index), and LPIPS (Zhang et al. (2018); Learned Perceptual Image  
 317 Patch Similarity), and additionally report frames per second (FPS) to assess rendering speed.  
 318

319 **Datasets.** We employ the CMU Panoptic Sports dataset (Joo et al., 2015) to validate scenarios  
 320 of fast motions with large inter-frame displacements in our experiments. Specifically, the Panoptic  
 321 Sports dataset is a challenging benchmark containing six sports scenes: juggle, basketball, boxing,  
 322 football, softball, and tennis. Each scene is recorded at 30 FPS for 5 seconds (150 frames per scene).  
 323 A total of 31 cameras were used, and the native resolution of  $640 \times 360$  was retained. Evaluation  
 324 was referenced to four fixed test cameras (IDs of 0, 10, 15, and 30).  
 325

326 **4DGS baselines.** We compare our method with recent 4DGS baselines across various strate-  
 327 gies, including (a) explicit parameterizations for 4DGS: 4DGS (Yang et al., 2024a), 4D-Rotor-  
 328

324 **Table 1: Comparisons on dynamic sports scenes in the CMU Panoptic Sports dataset.** We  
325 evaluate ours with existing 4DGS baselines on benchmarks containing fast motions with large inter-  
326 frame displacements. We report PSNR and SSIM for six sports scene sequences across all baselines.  
327

Method	4DGS Category	Basketball		Boxes		Football		Juggle		Softball		Tennis		Avg.			
		PSNR↑	SSIM↑	FPS↑	Storage↓												
Grid4D	Deformable	25.82	0.89	26.81	0.91	27.61	0.91	28.09	0.92	26.91	0.91	27.10	0.91	27.06	0.91	146	333
4DGaussian	Deformable	27.28	0.90	27.32	0.91	28.71	0.91	26.94	0.91	27.24	0.91	27.66	0.91	27.53	0.91	40	62
MoDec-GS	Deformable	27.42	0.90	26.17	0.92	27.09	0.92	28.03	0.93	27.31	0.92	27.36	0.92	27.23	0.92	62	34
TC3DGS	External supervision	27.92	0.89	28.28	0.89	28.00	0.89	29.15	0.90	27.96	0.89	25.97	0.89	27.88	0.89	890	49
D3DGS	External supervision	28.22	0.91	29.46	0.91	28.49	0.91	29.48	0.91	28.43	0.91	28.11	0.91	28.70	0.91	760	1994
4D-Rotor-Gaussians	Explicit	27.76	0.90	26.94	0.89	26.54	0.92	27.62	0.92	27.03	0.92	27.09	0.91	27.16	0.91	100	94
4DGS	Explicit	27.89	0.92	28.17	0.93	28.35	0.93	28.68	0.93	28.67	0.93	28.50	0.93	28.38	0.93	197	1293
Ours		<b>30.05</b>	<b>0.92</b>	<b>29.91</b>	<b>0.93</b>	<b>29.99</b>	<b>0.93</b>	<b>30.31</b>	<b>0.93</b>	<b>30.24</b>	<b>0.93</b>	<b>30.14</b>	<b>0.93</b>	<b>30.11</b>	<b>0.93</b>	104	1261



351 **Figure 4: Visualizations on dynamic sports scenes in the CMU Panoptic Sports dataset.** Com-  
352 pared to prior 4D Gaussian baselines, where fast-moving objects (e.g., ball, bat, and racket) often  
353 disappear or become corrupted, our method successfully preserves these objects throughout the se-  
354 quence, producing more faithful and consistent reconstructions.

355  
356 **Gaussians** (Duan et al., 2024)<sup>1</sup>, (b) deformable 4DGS: Grid4D (Xu et al., 2024), 4D Gaussian (Wu  
357 et al., 2024), MoDec-GS (Kwak et al., 2025), and (c) external supervision: D3DGS (Luiten et al.,  
358 2024), TC3DGS (Javed et al., 2024). We note that D3DGS and TC3DGS are designed to handle  
359 large inter-frame displacements, such as the Panoptic Sports dataset. All baselines are evaluated  
360 following the dynamic scene setups specified in their papers.

#### 362 4.1 EXPERIMENTAL RESULTS ON PANOPTIC SPORTS

363 In this section, we evaluate our method with various 4DGS baselines on six dynamic sports scenes  
364 (Basketball, Boxes, Football, Juggle, Softball, and Tennis) from the CMU Panoptic Sports dataset,  
365 which involve rapid human motions and small objects undergoing large inter-frame displacements.

366 As reported in Table 1, SPIN-4DGS achieves the best PSNR on all six scenes with an average  
367 of 30.11 dB, outperforming the strongest explicit baseline 4DGS (28.38 dB) by +1.73 dB and the  
368 external supervision baseline D3DGS (28.70 dB) by +1.41 dB. SSIM also remains consistently high  
369 at 0.93, confirming stable reconstruction quality. In particular, our method even surpasses models  
370 trained with external supervision such as segmentation maps (e.g., D3DGS, TC3DGS), showing that  
371 high fidelity can be achieved without costly priors. Beyond averages, the improvements are most  
372 significant on challenging scenes with extreme motion. On Basketball, SPIN-4DGS improves PSNR  
373 by over +1.83 dB against the best baseline, D3DGS (Luiten et al., 2024), while on Tennis, where  
374 rackets move rapidly and cover large displacements, the margin also surpasses +1.64 dB against  
375 the best baseline, 4DGS (Yang et al., 2024a). Overall, those results highlight the robustness of our  
376 approach to challenging fast-motion scenarios where prior methods often fail.

377 <sup>1</sup>We reimplemented the method using the official PyTorch code released by the authors.

378 Qualitative comparisons in Figure 4 further illustrate these differences. Deformable baseline (*i.e.*, 4DGaussian, first column) results blur fine-grained structures, explicit 4DGS (second) results frequently lose moving objects, and even externally supervised (*i.e.*, D3DGS, third) results suffer degradation on small, fast objects like a tennis racket. In contrast, SPIN-4DGS preserves sharp and stable reconstructions across all frames, closely matching the ground truth.

383 As shown in Figure 4, only the externally supervised baselines (*e.g.*, D3DGS) are able to represent  
 384 the fast-moving objects (*e.g.*, basketball) in these sports scenes. Although D3DGS achieves a high  
 385 rendering speed, it requires external supervision during training and incurs substantial storage over-  
 386 head (1994 MB) to store a large set of Gaussian attributes for the entire sequence. Explicit 4DGS  
 387 renders faster than SPIN-4DGS, yet still fails to reconstruct these fast-moving objects and yields  
 388 lower PSNR. In contrast, SPIN-4DGS attains higher fidelity with a smaller footprint (1261 MB) by  
 389 storing only Gaussian positions and the network. Such a network-based approach also makes it pos-  
 390 sible to reconstruct only selected time intervals without storing all Gaussians of the entire sequence.  
 391 Compared to other network-based deformable baselines, SPIN-4DGS reaches 104 FPS, substan-  
 392 tially higher than 4DGaussian (40 FPS) and MoDec-GS (62 FPS), while these methods still struggle  
 393 to represent fast-moving objects. These observations suggest that SPIN-4DGS offers a practically  
 394 usable trade-off among fidelity, storage, and speed for fast-motion sports scenes.

## 395 4.2 ABLATION STUDY AND ANALYSIS

397 We conduct a series of ablation experiments to demonstrate the proposed method further. First, we  
 398 analyze the impacts of estimated spatiotemporal position quality and refinement in Table 2 and 3.  
 399 We also examine a position-reuse setting in Table 4, where positions from existing 4DGS models  
 400 are provided, to validate the effectiveness of our attributes learning scheme. Finally, we validate the  
 401 effect of each component of our implicit network in Table 5.

403 **Table 2: Ablation study on spatiotemporal positions.** We perform ablation studies on (a) varying  
 404 the early training duration used to estimate spatiotemporal Gaussian positions from the explicit  
 405 baseline, 4DGS (Yang et al., 2024a), evaluated without subsequent refinement, and (b) varying the  
 406 number of frame-wise refinement iterations applied after position estimation.

(a) Effect of early training duration					(b) Effect of refinement iterations				
Iteration	PSNR↑	SSIM↑	LPIPS↓	Time↓	Iteration	PSNR↑	SSIM↑	LPIPS↓	Time↓
15K	<b>29.57</b>	<b>0.92</b>	<b>0.15</b>	<b>10m</b>	0.5K	29.86	0.92	0.14	33m
30K	29.39	0.91	<b>0.15</b>	30m	1K	29.89	0.92	0.14	55m
					2K	30.05	0.92	0.14	1h 40m

413 **Ablation on spatiotemporal positions.** We investigate how the quality of estimated spatiotemporal  
 414 positions and the amount of refinement affect the final reconstruction. Results are summarized in  
 415 Table 2, evaluated on the Basketball sequence.

416 (a) *Effect of early training duration.* Using positions extracted after 15K iterations of 4DGS (Yang  
 417 et al., 2024a) already achieves strong performance (29.57 PSNR, 0.92 SSIM) with only 10 minutes  
 418 of cost. Extending training to 30K iterations not only triples the runtime but also slightly degrades  
 419 the quality, indicating that long optimization is unnecessary once positions are sufficiently stable.

420 (b) *Effect of refinement iterations.* We then vary the number of frame-wise refinement steps after  
 421 position estimation. Increasing refinement from 0.5K to 2K iterations improves PSNR from 29.86  
 422 to 30.05, confirming that moderate refinement shows consistent benefits. In practice, we also prune  
 423 redundant Gaussians during refinement, which reduces background clutter and focuses updates on  
 424 salient regions, further enhancing efficiency.

426 **Effects of input position formulation.** We further analyze the effect of spatiotemporal slicing in  
 427 Table 3 and Figure 5. For a fair comparison, we fix the batch size to 1 and run all experiments on the  
 428 football sequence, varying only the position design. We compare two settings: (a) w/o spatiotempo-  
 429 ral slicing, where all Gaussians are optimized jointly without slicing, and (b) spatiotemporal slicing  
 430 (ours), where positions are sliced frame by frame and aligned along the time axis.

431 Without slicing, as shown in Table 3, Gaussians are optimized jointly in a unified 4D space. In this  
 formulation, a single Gaussian must simultaneously explain multiple timestamps. However, raster-

ization is performed frame by frame, so optimization that reduces the loss for one frame inevitably makes the Gaussian suboptimal for others. This cross-frame interference weakens the supervision signal, slows convergence, and increases both training time and memory usage. In contrast, spatiotemporal slicing explicitly separates Gaussians by  $(x, y, z, t)$  and filters out irrelevant points at each frame. This avoids interference across frames and ensures that optimization is focused on the relevant Gaussians for each time step. As a result, slicing achieves both higher reconstruction fidelity and significantly lower training cost.

Qualitative comparisons in Figure 5 confirm these findings. Under the unified 4D formulation, attributes collapse as Gaussians attempt to describe other timestamps, producing blurred faces and distorted fast-moving objects (e.g., football in the scene). Our sliced formulation decouples Gaussians over time, showing sharper details and temporally consistent reconstructions.

Table 3: **Ablation on spatiotemporal slicing.** We compare a unified 4D formulation (*i.e.*, w/o slicing), where Gaussian positions are optimized jointly across space–time, against our spatiotemporal slicing strategy that assigns positions per frame.

Spatiotemporal Slicing	PSNR↑	SSIM↑	Time↓	Train Cost↓
✗	27.48	0.89	1h 20m	18GB
✓	<b>28.96</b>	<b>0.92</b>	<b>25m</b>	<b>9GB</b>

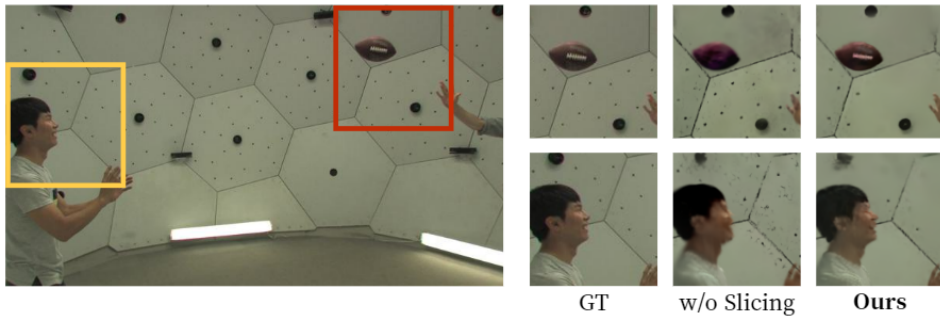


Figure 5: **Qualitative comparison of spatiotemporal slicing.** Without slicing, Gaussians simultaneously represent multiple time steps, causing their contributions to overlap and conflict during rasterization. This results in blurred faces and distorted fast-moving objects. Our slicing explicitly separates Gaussians over time, enhancing qualities with temporally consistent reconstructions.

**Impacts of implicit 4DGS scheme.** We further validate the impacts of the proposed implicit 4DGS scheme by reusing positions from strong baselines and retraining only attributes with our framework. In this setting, we extract pre-trained spatiotemporal positions from D3DGS (Luiten et al., 2024) and 4DGS (Yang et al., 2024a), but discard all their learned attributes. SPIN-4DGS then learns new attributes through its implicit network, while keeping the imported positions learnable to allow for refinement during training. This setup highlights not only the effectiveness of our attribute learning design but also its plug-and-play compatibility with existing 4DGS pipelines, where our scheme consistently enhances reconstruction quality regardless of the underlying position estimator.

Table 4: **Compatibility with existing 4DGS baselines.** We reuse pre-trained positions from D3DGS (Luiten et al., 2024) and 4DGS (Yang et al., 2024a), replacing their attribute optimization with our proposed implicit network training. SPIN-4DGS consistently improves PSNR/SSIM across all scenes, highlighting the compatibility and effectiveness of the proposed implicit 4DGS scheme.

Method	Basketball		Boxes		Football		Juggle		Softball		Tennis	
	PSNR↑	SSIM↑										
4DGS	27.89	<b>0.92</b>	28.17	<b>0.93</b>	28.35	<b>0.93</b>	28.68	<b>0.93</b>	28.67	<b>0.93</b>	28.50	<b>0.93</b>
4DGS + Ours	<b>29.57</b>	<b>0.92</b>	<b>29.63</b>	0.92	<b>29.42</b>	0.92	<b>29.98</b>	0.92	<b>29.94</b>	<b>0.93</b>	<b>29.83</b>	<b>0.93</b>
D3DGS	28.22	0.91	29.46	0.91	28.49	0.91	29.48	0.92	28.43	0.91	28.11	0.91
D3DGS + Ours	<b>30.50</b>	<b>0.94</b>	<b>30.26</b>	<b>0.94</b>	<b>29.21</b>	<b>0.94</b>	<b>31.04</b>	<b>0.95</b>	<b>30.92</b>	<b>0.95</b>	<b>30.51</b>	<b>0.95</b>

As shown in Table 4, SPIN-4DGS consistently improves performance even when initialized with external positions. With D3DGS positions, our method improves PSNR by +2.49 dB and SSIM to 0.95 on the *Softball* scene. Notably, while D3DGS collapses on *Tennis* (28.11/0.91), SPIN-4DGS still achieves 30.51/0.95 with sharp reconstructions. Even with 4DGS positions, our framework still

486 achieves consistent gains overall, demonstrating the effectiveness of the proposed scheme. While  
 487 SSIM occasionally drops slightly in some cases, we find that this minor loss is easily resolved by  
 488 our refinement step, showing that performance remains robust and stable.

489 We find that high-quality positions alone are insufficient for stable reconstructions, as attributes play  
 490 a critical role in maintaining fidelity under large inter-frame displacements. We also observe that  
 491 our implicit 4DGS formulation generalizes seamlessly across different baselines, showing strong  
 492 compatibility and consistent improvements regardless of the source of positions. Taken together,  
 493 these results highlight SPIN-4DGS as an effective and extensible 4DGS scheme that can enhance a  
 494 wide range of dynamic scene reconstruction tasks.

495  
 496 **Table 5: Ablation on our implicit network design components.** Starting from the original 4D  
 497 hash encoder (Chen et al., 2025), we analyze the effects of making positions trainable, applying  
 498 input position normalization, and changing activation functions. Each modification progressively  
 499 enhances reconstruction quality. All experiments are performed on the Basketball scene.

Network Components				Results		
Trainable position	Normalization	Activation	Hash Map Size	PSNR↑	SSIM↑	LPIPS↓
		ReLU	21	18.64	0.78	0.45
✓		ReLU	21	19.17	0.78	0.46
✓	✓	ReLU	21	29.89	0.92	0.16
✓	✓	GELU	21	30.05	0.92	0.14
✓	✓	GELU	23	<b>30.25</b>	<b>0.93</b>	<b>0.13</b>

500  
 501 **Component analysis.** We conduct an ablation study on the design components of our implicit  
 502 network, summarized in Table 5. Starting from the original 4D hash encoder (Chen et al., 2025)  
 503 encoder with fixed positions and ReLU activations, reconstruction quality is notably poor (18.64  
 504 PSNR, 0.78 SSIM, 0.45 LPIPS). Making positions trainable alone achieves only marginal improve-  
 505 ment, indicating that position refinement is insufficient without additional modifications. Applying  
 506 input position normalization shows a significant gain, boosting PSNR by over +10 dB and reduc-  
 507 ing LPIPS from 0.45 to 0.16, highlighting its importance for stabilized training. Replacing ReLU  
 508 with GELU further improves fidelity, enlarging the hash map size further achieves the best overall  
 509 performances (30.25 PSNR, 0.93 SSIM, 0.13 LPIPS). These results confirm that each component  
 510 contributes to stability and accuracy, with their combination being crucial for achieving high-quality  
 511 reconstructions.

## 5 CONCLUSION

520 In this work, we addressed the challenge of dynamic scene reconstruction under fast motions with  
 521 large inter-frame displacements. Existing 4DGS methods, including deformable and explicit  
 522 approaches, often fail to maintain Gaussian attributes in such regimes, resulting in blurred or vanished  
 523 objects. We introduced SPIN-4DGS, a new framework that learns Gaussian attributes directly from  
 524 explicit spatiotemporal positions via a feed-forward network, rather than relying on temporal dis-  
 525 placement modeling. By decoupling Gaussian position estimation from Gaussian attribute learning,  
 526 SPIN-4DGS offers a simple yet effective design principle for representing dynamic scenes under  
 527 fast motions. SPIN-4DGS achieved high-quality reconstructions of fast-moving objects under large  
 528 inter-frame displacements, as demonstrated through extensive experiments across dynamic sports  
 529 scenes in the CMU Panoptic Sports dataset. Overall, we believe SPIN-4DGS advances 4D Gaussian  
 530 Splatting toward practical deployment in challenging real-world scenarios.

## 533 REFERENCES

534  
 535 Abien Fred Agarap. Deep learning using rectified linear units (relu). *arXiv preprint*  
 536 *arXiv:1803.08375*, 2018.  
 537  
 538 Jeongmin Bae, Seoha Kim, Youngsik Yun, Hahyun Lee, Gun Bang, and Youngjung Uh. Per-  
 539 gaussian embedding-based deformation for deformable 3d gaussian splatting. In *European Con-  
 ference on Computer Vision*, pp. 321–335. Springer, 2024.

540 Jonathan T. Barron, Ben Mildenhall, Matthew Tancik, Peter Hedman, Ricardo Martin-Brualla, and  
 541 Pratul P. Srinivasan. Mip-nerf: A multiscale representation for anti-aliasing neural radiance fields,  
 542 2021.

543 Ang Cao and Justin Johnson. Hexplane: A fast representation for dynamic scenes. In *Proceedings*  
 544 of the IEEE/CVF Conference on Computer Vision and Pattern Recognition, pp. 130–141, 2023.

545 Jie Chen, Zhangchi Hu, Peixi Wu, Huyue Zhu, Hebei Li, and Xiaoyan Sun. Dash: Self-supervised  
 546 decomposition and 4d hash encoding for real-time dynamic scene rendering. In *International*  
 547 *Conference on Computer Vision (ICCV)*, 2025.

548 Pinxuan Dai, Peiquan Zhang, Zheng Dong, Ke Xu, Yifan Peng, Dandan Ding, Yujun Shen, Yin  
 549 Yang, Xinguo Liu, Rynson WH Lau, et al. 4d gaussian videos with motion layering. *ACM*  
 550 *Transactions on Graphics (TOG)*, 44(4):1–14, 2025.

551 Yuanxing Duan, Fangyin Wei, Qiyu Dai, Yuhang He, Wenzheng Chen, and Baoquan Chen. 4d-  
 552 rotor gaussian splatting: towards efficient novel view synthesis for dynamic scenes. In *ACM*  
 553 *SIGGRAPH 2024 Conference Papers*, pp. 1–11, 2024.

554 Sara Fridovich-Keil, Giacomo Meanti, Frederik Rahbæk Warburg, Benjamin Recht, and Angjoo  
 555 Kanazawa. K-planes: Explicit radiance fields in space, time, and appearance. In *Proceedings* of  
 556 the IEEE/CVF Conference on Computer Vision and Pattern Recognition, pp. 12479–12488, 2023.

557 Dan Hendrycks and Kevin Gimpel. Gaussian error linear units (gelus). *arXiv preprint*  
 558 *arXiv:1606.08415*, 2016.

559 Saqib Javed, Ahmad Jarrar Khan, Corentin Dumery, Chen Zhao, and Mathieu Salzmann. Temporally  
 560 compressed 3d gaussian splatting for dynamic scenes. *arXiv preprint arXiv:2412.05700*, 2024.

561 Hanbyul Joo, Hao Liu, Lei Tan, Lin Gui, Bart Nabbe, Iain Matthews, Takeo Kanade, Shohei  
 562 Nobuhara, and Yaser Sheikh. Panoptic studio: A massively multiview system for social motion  
 563 capture. In *Proceedings of the IEEE international conference on computer vision*, pp. 3334–3342,  
 564 2015.

565 Bernhard Kerbl, Georgios Kopanas, Thomas Leimkühler, and George Drettakis. 3d gaussian splat-  
 566 ting for real-time radiance field rendering. *ACM Transactions on Graphics*, 42(4), July 2023.

567 Diederik Kinga, Jimmy Ba Adam, et al. A method for stochastic optimization. In *International*  
 568 *conference on learning representations (ICLR)*, volume 5. California;, 2015.

569 Sangwoon Kwak, Joonsoo Kim, Jun Young Jeong, Won-Sik Cheong, Jihyong Oh, and Munchurl  
 570 Kim. Modec-gs: Global-to-local motion decomposition and temporal interval adjustment for  
 571 compact dynamic 3d gaussian splatting. In *Proceedings of the Computer Vision and Pattern*  
 572 *Recognition Conference*, pp. 11338–11348, 2025.

573 Junoh Lee, Chang Yeon Won, Hyunjun Jung, Inhwan Bae, and Hae-Gon Jeon. Fully explicit dynamic  
 574 gaussian splatting. *Advances in Neural Information Processing Systems*, 37:5384–5409, 2024.

575 Minseo Lee, Byeonghyeon Lee, Lucas Yunkyu Lee, Eunsoo Lee, Sangmin Kim, Seunghyeon Song,  
 576 Joo Chan Lee, Jong Hwan Ko, Jaesik Park, and Eunbyung Park. Optimized minimal 4d gaussian  
 577 splatting, 2025. URL <https://arxiv.org/abs/2510.03857>.

578 Lingzhi Li, Zhen Shen, Zhongshu Wang, Li Shen, and Ping Tan. Streaming radiance fields for 3d  
 579 video synthesis. *Advances in Neural Information Processing Systems*, 35:13485–13498, 2022a.

580 Tianye Li, Mira Slavcheva, Michael Zollhoefer, Simon Green, Christoph Lassner, Changil Kim,  
 581 Tanner Schmidt, Steven Lovegrove, Michael Goesele, Richard Newcombe, et al. Neural 3d video  
 582 synthesis from multi-view video. In *Proceedings of the IEEE/CVF conference on computer vision*  
 583 and pattern recognition, pp. 5521–5531, 2022b.

584 Youtian Lin, Zuozhuo Dai, Siyu Zhu, and Yao Yao. Gaussian-flow: 4d reconstruction with dy-  
 585 namic 3d gaussian particle. In *Proceedings of the IEEE/CVF Conference on Computer Vision and*  
 586 *Pattern Recognition*, pp. 21136–21145, 2024.

594 Zhicheng Lu, Xiang Guo, Le Hui, Tianrui Chen, Min Yang, Xiao Tang, Feng Zhu, and Yuchao Dai.  
 595 3d geometry-aware deformable gaussian splatting for dynamic view synthesis. In *Proceedings of*  
 596 *the IEEE/CVF Conference on Computer Vision and Pattern Recognition*, pp. 8900–8910, 2024.

597 Jonathon Luiten, Georgios Kopanas, Bastian Leibe, and Deva Ramanan. Dynamic 3d gaussians:  
 598 Tracking by persistent dynamic view synthesis. In *2024 International Conference on 3D Vision*  
 599 (*3DV*), pp. 800–809. IEEE, 2024.

600 Jipeng Lyu, Jiahua Dong, and Yu-Xiong Wang. SCas4d: Structural cascaded optimization for boost-  
 601 ing persistent 4d novel view synthesis. *Transactions on Machine Learning Research*, 2025. ISSN  
 602 2835-8856. Featured Certification.

603 Thomas Müller, Alex Evans, Christoph Schied, and Alexander Keller. Instant neural graphics primitives with a multiresolution hash encoding. *ACM Transactions on Graphics*, 41(4):1–15, July  
 604 2022. ISSN 1557-7368. doi: 10.1145/3528223.3530127.

605 Seungjun Oh, Younggeun Lee, Hyejin Jeon, and Eunbyung Park. Hybrid 3d-4d gaussian splatting  
 606 for fast dynamic scene representation. *arXiv preprint arXiv:2505.13215*, 2025.

607 Keunhong Park, Utkarsh Sinha, Jonathan T. Barron, Sofien Bouaziz, Dan B Goldman, Steven M.  
 608 Seitz, and Ricardo Martin-Brualla. Nerfies: Deformable neural radiance fields. *ICCV*, 2021.

609 Adam Paszke, Sam Gross, Francisco Massa, Adam Lerer, James Bradbury, Gregory Chanan, Trevor  
 610 Killeen, Zeming Lin, Natalia Gimelshein, Luca Antiga, Alban Desmaison, Andreas Kopf, Edward  
 611 Yang, Zachary DeVito, Martin Raison, Alykhan Tejani, Sasank Chilamkurthy, Benoit Steiner,  
 612 Lu Fang, Junjie Bai, and Soumith Chintala. Pytorch: An imperative style, high-performance  
 613 deep learning library. In *Advances in Neural Information Processing Systems 32*, pp. 8024–8035.  
 614 Curran Associates, Inc., 2019.

615 Johannes L Schonberger and Jan-Michael Frahm. Structure-from-motion revisited. In *Proceedings*  
 616 *of the IEEE conference on computer vision and pattern recognition*, pp. 4104–4113, 2016.

617 Jiakai Sun, Han Jiao, Guangyuan Li, Zhanjie Zhang, Lei Zhao, and Wei Xing. 3dgstream: On-the-  
 618 fly training of 3d gaussians for efficient streaming of photo-realistic free-viewpoint videos. In  
 619 *Proceedings of the IEEE/CVF Conference on Computer Vision and Pattern Recognition (CVPR)*,  
 620 pp. 20675–20685, June 2024.

621 Zhou Wang, Alan C Bovik, Hamid R Sheikh, and Eero P Simoncelli. Image quality assessment:  
 622 from error visibility to structural similarity. *IEEE transactions on image processing*, 13(4):600–  
 623 612, 2004.

624 Guanjun Wu, Taoran Yi, Jiemin Fang, Lingxi Xie, Xiaopeng Zhang, Wei Wei, Wenyu Liu, Qi Tian,  
 625 and Xinggang Wang. 4d gaussian splatting for real-time dynamic scene rendering. In *Proceedings*  
 626 *of the IEEE/CVF conference on computer vision and pattern recognition*, pp. 20310–20320, 2024.

627 Jiawei Xu, Zexin Fan, Jian Yang, and Jin Xie. Grid4d: 4d decomposed hash encoding for high-  
 628 fidelity dynamic gaussian splatting. *Advances in Neural Information Processing Systems*, 37:  
 629 123787–123811, 2024.

630 Zeyu Yang, Hongye Yang, Zijie Pan, and Li Zhang. Real-time photorealistic dynamic scene rep-  
 631 resentation and rendering with 4d gaussian splatting. In *International Conference on Learning*  
 632 *Representations (ICLR)*, 2024a.

633 Ziyi Yang, Xinyu Gao, Wen Zhou, Shaohui Jiao, Yuqing Zhang, and Xiaogang Jin. Deformable  
 634 3d gaussians for high-fidelity monocular dynamic scene reconstruction. In *Proceedings of the*  
 635 *IEEE/CVF conference on computer vision and pattern recognition*, pp. 20331–20341, 2024b.

636 Richard Zhang, Phillip Isola, Alexei A Efros, Eli Shechtman, and Oliver Wang. The unreasonable  
 637 effectiveness of deep features as a perceptual metric. In *Proceedings of the IEEE conference on*  
 638 *computer vision and pattern recognition*, pp. 586–595, 2018.

639 Ruijie Zhu, Yanzhe Liang, Hanzhi Chang, Jiacheng Deng, Jiahao Lu, Wenfei Yang, Tianzhu Zhang,  
 640 and Yongdong Zhang. Motions: Exploring explicit motion guidance for deformable 3d gaussian  
 641 splatting. *Advances in Neural Information Processing Systems*, 37:101790–101817, 2024.

648 Matthias Zwicker, Hanspeter Pfister, Jeroen Van Baar, and Markus Gross. Ewa volume splatting. In  
649 *Proceedings Visualization, 2001. VIS'01.*, pp. 29–538. IEEE, 2001.  
650  
651  
652  
653  
654  
655  
656  
657  
658  
659  
660  
661  
662  
663  
664  
665  
666  
667  
668  
669  
670  
671  
672  
673  
674  
675  
676  
677  
678  
679  
680  
681  
682  
683  
684  
685  
686  
687  
688  
689  
690  
691  
692  
693  
694  
695  
696  
697  
698  
699  
700  
701

702  
703  

## A MORE ABLATION STUDIES

704  
705  
706  
707  
708  
709  
710  

**Perceptual quality comparison.** In terms of perceptual quality (LPIPS), SPIN-4DGS also delivers competitive performance across all six scenes on the CMU dataset. As shown in Table 6, our method achieves a mean LPIPS of 0.14, substantially improving over the strongest baseline D3DGS (0.18) while remaining close to the explicit baseline 4DGS (0.13). These results indicate that SPIN-4DGS effectively suppresses blur and collapse artifacts around fast-moving objects without sacrificing perceptual fidelity, and together with the PSNR/SSIM gains further confirm the robustness of our method under challenging fast-motion scenarios.

711  
712  
713  

Table 6: **Perceptual quality comparison.** We report LPIPS across six sports scenes on the CMU Panoptic Sports dataset. Lower scores indicate better perceptual quality.

714  
715  
716  
717  
718  
719  

Model	4DGS Category	Basketball	Boxes	Football	Juggle	Softball	Tennis	Avg.
D3DGS	External supervision	0.18	0.17	0.19	0.15	0.19	0.17	0.18
4DGS	Explicit	<b>0.14</b>	<b>0.12</b>	<b>0.13</b>	<b>0.12</b>	<b>0.12</b>	<b>0.13</b>	<b>0.13</b>
Ours	-	<b>0.14</b>	0.14	0.14	0.13	0.13	<b>0.13</b>	0.14

720  
721  
722  
723  
724  
725  
726  
727  
728  
729  

**Training budget.** Compared to the strongest baseline D3DGS, SPIN-4DGS offers a better trade-off between reconstruction quality and training time, as summarized in Table 7. With a lightweight 15K-iteration configuration without refinement, SPIN-4DGS already attains 28.82 dB on Basketball, outperforming D3DGS (28.22 dB) while reducing training time from 100 to 45 minutes. Adding a short refinement stage (15K position iterations and 0.5K refinement iterations) further improves PSNR to 29.13 dB in 73 minutes, still faster than D3DGS. With more compute, longer refinement yields additional gains: 15K + 2K reaches 29.51 dB in 142 minutes, and the full 40K + 2K setting achieves 30.05 dB in 195 minutes, *i.e.*, +1.83 dB over D3DGS. Overall, our two-stage design can match or surpass D3DGS with a substantially smaller training budget (even without external supervision), while providing a smooth path to higher fidelity when more budget is available.

730  
731  
732  
733  

Table 7: **Training time breakdown and PSNR on the Basketball scene.** We compare PSNR, position-estimation time, refinement cost, network training time, and total training time across different SPIN-4DGS configurations and the D3DGS baseline. All time measurements are reported in minutes.

734  
735  
736  
737  
738  
739  
740  
741  
742  

Method	Setting	PSNR	Position	Refine	Network	Total time
D3DGS	Default	28.22	—	—	—	100
Ours	15K, No refine	28.82	10	0	35	45
	15K, Refine (0.5K)	29.13	10	33	30	73
	15K, Refine (2K)	29.51	10	100	32	142
	40K, Refine (2K)	30.05	10	100	85	195

743  
744  
745  
746  
747  
748  
749  
750  
751  
752  
753  
754  
755  

**Neu3DV benchmark.** We additionally evaluate SPIN-4DGS on the Neu3DV(Li et al., 2022b) benchmark, which features complex backgrounds and smaller motions. In this experiment, we keep the default SPIN-4DGS training setup without the refinement stage, training only on pre-refinement spatiotemporal positions, with the hash map size hyperparameter set to 23 throughout training. As summarized in Table 8, SPIN-4DGS attains the highest average PSNR of 32.19 dB, slightly outperforming the strongest explicit baseline 4DGS (32.01 dB) by +0.18 dB and clearly improving over deformable methods such as Grid4D (31.49 dB) by +0.70 dB and 4DGaussian (31.01 dB) by +1.18 dB. Moreover, SPIN-4DGS improves over the externally supervised D3DGS baseline (31.04 dB) by 1.15 dB in mean PSNR, and SSIM also remains consistently high at 0.95, matching or surpassing the best competing methods. Qualitative comparisons in Figure 9 show that moving objects (*e.g.*, the tongs and knife) appear blurred or smeared with 4DGS, whereas SPIN-4DGS reconstructs them with much sharper details, confirming stable reconstruction quality on complex, slower-motion scenes.

**MeetRoom benchmark.** We further evaluate SPIN-4DGS on the three scenes (Discussion, Trimming, VR Headset) from the MeetRoom benchmark (Li et al., 2022a), which contain cluttered indoor

756 **Table 8: Comparisons on the Neu3DV scenes.** We report PSNR (and SSIM when available) for  
 757 SPIN-4DGS and baselines across six sequences.

759 Method	4DGS Category	760 Coffee Martini		761 Cook Spinach		762 Cut Roasted Beef		763 Flame Salmon		764 Flame Steak		765 Sear Steak		766 Avg.	
		767 PSNR↑	768 SSIM↑	769 PSNR↑	770 SSIM↑	771 PSNR↑	772 SSIM↑	773 PSNR↑	774 SSIM↑	775 PSNR↑	776 SSIM↑	777 PSNR↑	778 SSIM↑	779 PSNR↑	780 SSIM↑
Grid4D (Xu et al., 2024)	Deformable	28.30	0.90	32.58	0.95	33.22	0.95	29.12	0.91	32.56	<b>0.96</b>	33.16	<b>0.96</b>	31.49	0.94
4DGaussian (Wu et al., 2024)	Deformable	27.34	0.90	32.50	0.94	32.26	0.94	27.99	0.90	32.54	0.95	33.44	0.95	31.01	0.93
D3DGS (Luiten et al., 2024)	External supervision	27.32	-	32.97	-	31.75	-	27.26	-	33.24	-	33.68	-	31.04	-
4DGS (Yang et al., 2024a)	Explicit	-	-	32.93	-	33.85	-	<b>29.38</b>	-	<b>34.03</b>	-	33.51	-	32.01	-
4DGS(re-impl.) (Lee et al., 2025)	Explicit	27.92	<b>0.92</b>	33.58	<b>0.96</b>	33.96	<b>0.96</b>	28.72	<b>0.92</b>	33.96	<b>0.96</b>	33.61	<b>0.96</b>	31.96	<b>0.95</b>
Ours	-	<b>28.42</b>	<b>0.92</b>	<b>33.61</b>	<b>0.96</b>	<b>34.05</b>	<b>0.96</b>	28.97	<b>0.92</b>	33.96	<b>0.96</b>	<b>34.14</b>	<b>0.96</b>	<b>32.19</b>	<b>0.95</b>

766 backgrounds and relatively small motions. Using the same configuration as in our main experiments,  
 767 we train SPIN-4DGS only on the pre-refinement spatiotemporal positions, with the hash-map size  
 768 fixed to 23 throughout training. Table 9 shows that SPIN-4DGS consistently achieves higher PSNR  
 769 than all baselines, including StreamRF (26.72 dB), 3DGStream (30.79 dB), and 4DGS (30.47 dB).  
 770 Overall, it provides an average improvement of +1.6 dB over the explicit 4DGS baseline. In par-  
 771 ticular, on the Trimming scene, SPIN-4DGS attains 32.41 dB, improving over the explicit 4DGS  
 772 baseline (30.16 dB) by more than 2 dB, while also maintaining a high SSIM of 0.96. Qualitative  
 773 comparisons in Figure 10 illustrate these effects: while 4DGS-based baselines often fail to faithfully  
 774 reconstruct objects due to noise and artifacts in both the foreground and background, SPIN-4DGS  
 775 yields sharper object reconstructions and substantially cleaner backgrounds. These results suggest  
 776 that our model remains robust even in indoor scenes with cluttered backgrounds and relatively small  
 777 motions.

778 **Table 9: Comparisons on the MeetRoom scenes.** We report PSNR and SSIM for SPIN-4DGS  
 779 and baselines across three sequences and their average. Note that only average PSNR scores are  
 780 available for StreamRF and 3DGStream.

781 Method	782 Category	783 Discussion		784 Trimming		785 VR Headset		786 AVG	
		787 PSNR↑	788 SSIM↑	789 PSNR↑	790 SSIM↑	791 PSNR↑	792 SSIM↑	793 PSNR↑	794 SSIM↑
StreamRF (Li et al., 2022a)	Implicit	-	-	-	-	-	-	26.72	-
3DGStream (Sun et al., 2024)	Explicit	-	-	-	-	-	-	30.79	-
4DGS (Yang et al., 2024a)	Explicit	31.51	<b>0.96</b>	30.16	0.94	29.74	<b>0.95</b>	30.47	0.95
Ours	-	<b>32.30</b>	<b>0.96</b>	<b>32.41</b>	<b>0.96</b>	<b>31.42</b>	<b>0.95</b>	<b>32.04</b>	<b>0.96</b>

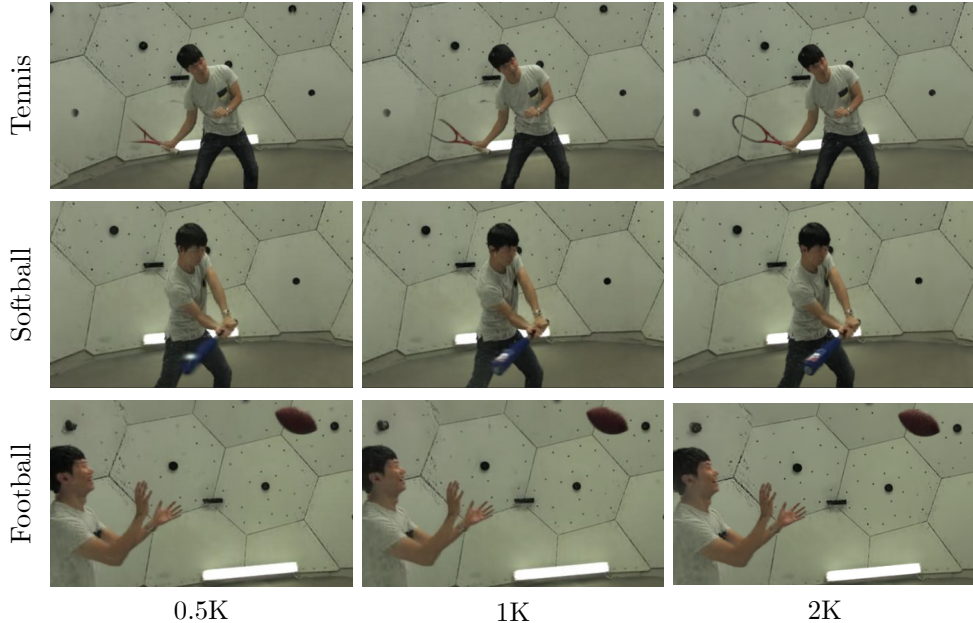
788 **Comparison to frame-wise 3DGS.** To verify the benefits of our temporally shared implicit repre-  
 789 sentation over frame-wise 3DGS (*i.e.*, a collection of 3DGS on each frame), we directly compared  
 790 SPIN-4DGS with frame-wise 3DGS (Kerbl et al., 2023) and D3DGS (Luiten et al., 2024) on the  
 791 CMU Panoptic Sports benchmark, where we referred to the results reported in the D3DGS (Luiten  
 792 et al., 2024). Table 10 shows that SPIN-4DGS achieves the best performance on all six CMU Panop-  
 793 tic Sports scenes, surpassing both frame-wise 3DGS and D3DGS. Quantitatively, SPIN-4DGS im-  
 794 proves PSNR by 1.9dB on average frame-wise 3DGS and with gains of up to +3.03dB on *Basketball*.  
 795 These substantial gains suggest that our temporally shared implicit field can better exploit temporal  
 796 regularities and cross-frame correlations, yielding a more coherent 4D representation than a set of  
 797 independently optimized frame-wise 3DGS models.

## B MORE QUALITATIVE RESULTS

801 **Qualitative results on spatiotemporal position refinement.** Figure 6 visualizes the ablation  
 802 study on the position refinement in Table 2. With only 0.5K refinement iterations, SPIN-4DGS  
 803 already captures stable object structures without collapse, while increasing iterations to 1K and 2K  
 804 further improves fine details such as ball edges and racket nets. Specifically, our refinement stage  
 805 employs Gaussian densification, which both allocates new Gaussians in regions that lack detail and  
 806 prunes redundant ones, incrementally filling in missing structures while reducing the number of  
 807 unnecessary Gaussians. This process can alleviate the dependence on initially collected positions,  
 808 allowing SPIN-4DGS to train on a reliable input point set. These results indicate that SPIN-4DGS is  
 809 effective even with minimal refinement budgets and that additional iterations mainly serve to sharpen  
 810 fine details rather than prevent collapse.

810  
 811 **Table 10: Comparison with frame-wise 3DGS on the CMU Panoptic Sports benchmark.** We  
 812 report PSNR across six sports, showing that SPIN-4DGS consistently outperforms both 3DGS and  
 813 D3DGS across all sequences.

Model	Basketball	Boxes	Football	Juggle	Softball	Tennis	Avg.
3DGS	27.02	28.74	28.49	28.19	28.77	28.03	28.21
D3DGS	28.22	29.46	28.49	29.48	28.43	28.11	28.70
Ours	<b>30.05</b>	<b>29.91</b>	<b>29.99</b>	<b>30.31</b>	<b>30.24</b>	<b>30.14</b>	<b>30.11</b>



840 **Figure 6: Visualizations on spatiotemporal position refinement.** We visualize the effect of vary-  
 841 ing refinement iterations (0.5K, 1K, 2K) corresponding to Table 2b. Even with only 0.5K iterations,  
 842 SPIN-4DGS retains consistent object structures without collapse, while progressively increasing the  
 843 number of iterations recovers fine details such as ball edges and racket nets.

844  
 845 **Qualitative results with various baselines.** Figure 7 shows qualitative comparisons on the CMU  
 846 Panoptic Sports dataset for two baseline methods in Table 1: MoDec-GS and 4D-Rotor-Gaussians.  
 847 For MoDec-GS, while the background remains relatively stable, the player becomes heavily blurred  
 848 and fast-moving objects (*e.g.*, basketball, tennis racket) are often not reconstructed correctly, similar  
 849 to prior deformable 4DGS approaches. 4D-Rotor-Gaussians retains these objects more reliably, but  
 850 still exhibits noticeable blur and geometry instability of the player under fast motion. In contrast,  
 851 SPIN-4DGS reconstructs both the moving objects and the player with sharp and temporally stable  
 852 geometry, yielding visually cleaner and more consistent results than both baselines.

853 **Qualitative results on compatibility with existing 4DGS baselines.** Figure 8 presents qualita-  
 854 tive results for the compatibility study in Table 4. Across scenes, our method reconstructs stable  
 855 backgrounds and more temporally consistent details, while the original baselines often blur or lose  
 856 fast-moving objects. These results confirm that the proposed scheme integrates effectively with  
 857 existing 4DGS approaches and potentially improves their reconstruction fidelity under large inter-  
 858 frame displacements.

## C DISCUSSIONS

862 **Recent trends in 4DGS.** Recent concurrent 4DGS methods (Dai et al., 2025; Oh et al., 2025; Lyu  
 863 et al., 2025) have been introduced, often sharing similar architectural components but pursuing dif-  
 ferent goals and design constraints than ours. 4DGV (Dai et al., 2025) focuses on reducing model

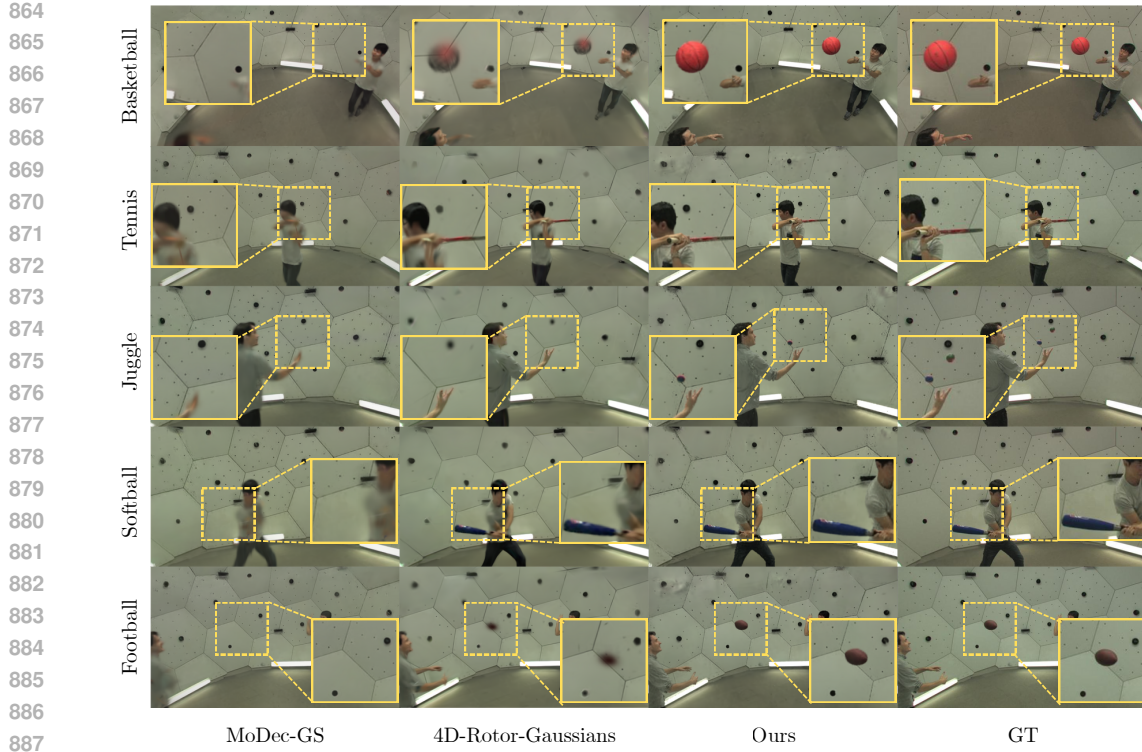


Figure 7: **Visualization on dynamic sports scenes in the CMU Panoptic Sports dataset.** We visualize the methods evaluated in Table 1, including MoDec-GS and 4D-Rotor-Gaussians. These 4DGS baselines often exhibit geometry instability and fast-motion artifacts, whereas SPIN-4DGS preserves the object and player geometry sharply throughout the sequence.

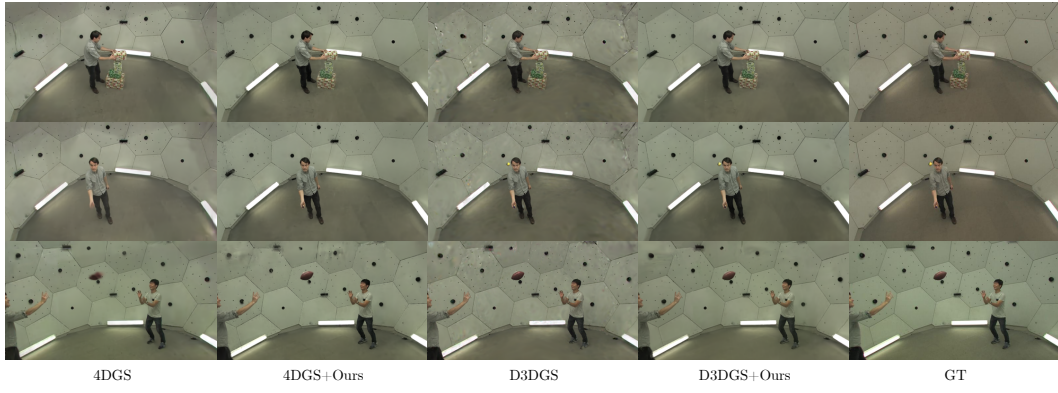
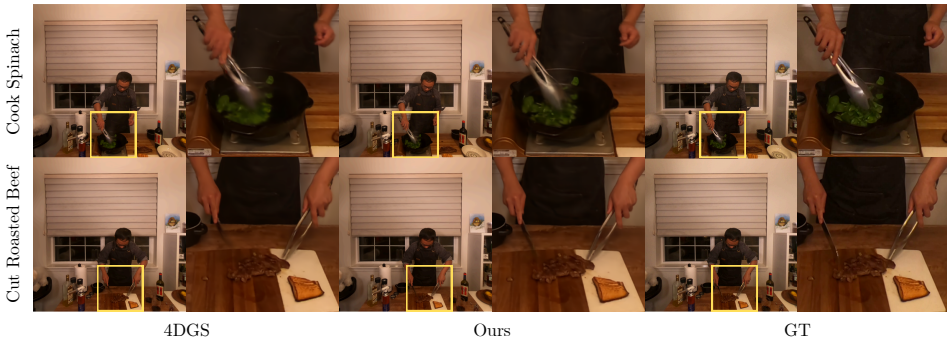
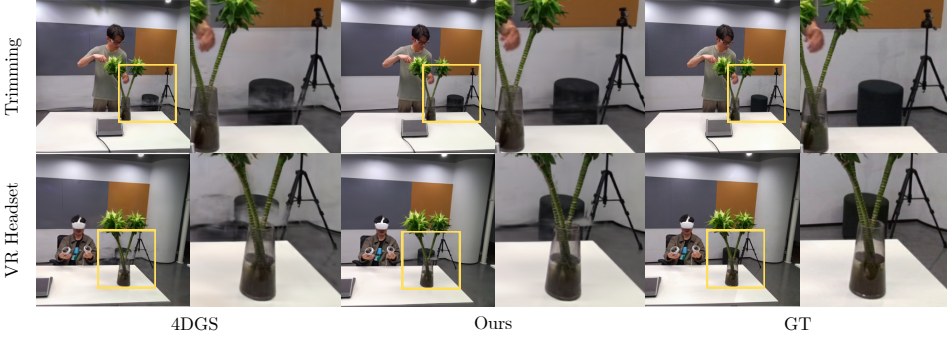


Figure 8: **Visualizations on compatibility with existing 4DGS baselines.** We visualize the results of compatibility ablation study in Table 4, where pre-trained positions from 4DGS and D3DGS are reused while attributes are retrained with SPIN-4DGS. Our method consistently produces clear and more stable reconstructions than the original baselines.

size for complex dynamic scenes by leveraging external 2D segmentation, thereby relying on external supervision. Hybrid 3D-4DGS (Oh et al., 2025) builds upon 4DGS and mitigates redundancy in static regions by converting Gaussians that barely change over time into 3D ones; however, dynamic Gaussians are still shared across multiple frames, leaving cross-frame interference unresolved for fast motions. SCas4D (Lyu et al., 2025), built on Dynamic3DGS, accelerates online 4D reconstruction via cluster-wise shared transformations, but this design couples all Gaussians within a cluster to a single motion model and makes the method sensitive to the initial K-means clustering. By contrast, SPIN-4DGS directly predicts frame-wise attributes from explicit spatiotemporal positions



918  
919  
920  
921  
922  
923  
924  
925  
926  
927  
928  
929  
930  
931  
932  
933  
934  
935  
936  
937  
938  
939  
940  
941  
942  
943  
944  
945  
946  
947  
948  
949  
950  
951  
952  
953  
954  
955  
956  
957  
958  
959  
960  
961  
962  
963  
964  
965  
966  
967  
968  
969  
970  
971  
Figure 9: **Qualitative comparison on the Neu3DV benchmark.** We visualize representative results from two Neu3DV scenes (*e.g.*, Cook Spinach and Cut Roasted Beef) reported in Table 8. 4DGS blurs the boundaries of moving objects (*e.g.*, tongs and knife), whereas SPIN-4DGS achieves significantly cleaner and higher-fidelity reconstructions.



946  
947  
948  
949  
950  
951  
952  
953  
954  
955  
956  
957  
958  
959  
960  
961  
962  
963  
964  
965  
966  
967  
968  
969  
970  
971  
Figure 10: **Qualitative comparison on the MeetRoom benchmark.** We visualize representative results from two MeetRoom scenes (*e.g.*, Trimming and VR Headset) reported in Table 9. The 4DGS exhibit noticeable background noise and often fail to reconstruct the foreground objects faithfully, whereas SPIN-4DGS achieves sharper object reconstruction with substantially cleaner backgrounds.

with an implicit decoder, avoiding cross-frame interference and enabling stable reconstruction of fast motions without requiring external supervision or cluster-based initialization.

**Key differences from prior 4DGS.** The key conceptual difference between SPIN-4DGS and prior 4DGS methods is how temporal appearance is parameterized. SPIN-4DGS rasterizes each frame from explicit spatiotemporal positions and predicts Gaussian attributes as a function of the spatiotemporal coordinates via  $f_\theta(\mathbf{u}, t)$ . This design keeps positions explicit, allows only light per-sample adjustments during training, and decouples attribute optimization across timesteps, so different samples can receive different attributes without directly sharing a single attribute vector over time.

In contrast, standard explicit 4DGS (*e.g.*, 4DGS, 4D-Rotor-Gaussians) generate each frame by time-slicing a 4D primitive, and deformable 4DGS transform canonical Gaussians over time; in both cases, multiple timesteps share the same underlying Gaussian attributes. As a result, a single set of Gaussian attributes (or transforms) simultaneously influences multiple frames, and updates driven by one frame can easily degrade others under large inter-frame displacements, leading to temporal collapse of fast-moving objects. Our temporal parameterization breaks this coupling at the attribute level and instead places the temporal representation in  $f_\theta$  rather than in a pointwise deformation field. As shown in Table 1, this leads to more stable training under large inter-frame displacements and yields higher reconstruction quality (PSNR/SSIM) on fast-motion scenes.

Moreover, several deformable 4DGS methods deliberately avoid time-varying color and opacity, as allowing these attributes to change over time often produces unstable or implausible surfaces in novel views and makes tracking difficult. By predicting color and opacity from spatiotempo-

972 ral coordinates through  $f_\theta$  while keeping the underlying Gaussian support stable, SPIN-4DGS can  
973 model genuinely time-varying appearance without sacrificing temporal stability, which is crucial for  
974 fast-moving objects with large inter-frame displacements.

975 **Limitations.** We empirically observe that our method is most effective when a sufficiently dense  
976 set of spatiotemporal positions is available. In large-scale outdoor or highly cluttered scenes with  
977 sparse initial positions, achieving high reconstruction quality may require longer refinement (den-  
978 sify/prune) schedules to allocate more Gaussians, thereby increasing the overall training cost. In  
979 addition, for small objects or regions with very few initial points, we empirically observe that even  
980 multiple refinement iterations struggle to generate or recover sufficient missing points.

981 **LLM policy.** LLMs were used only for editing (grammar and typographical errors) and did not  
982 contribute to idea generation, analysis, experimental design, or interpretation.

984  
985  
986  
987  
988  
989  
990  
991  
992  
993  
994  
995  
996  
997  
998  
999  
1000  
1001  
1002  
1003  
1004  
1005  
1006  
1007  
1008  
1009  
1010  
1011  
1012  
1013  
1014  
1015  
1016  
1017  
1018  
1019  
1020  
1021  
1022  
1023  
1024  
1025